JACS
JOURNAL OF THE AMERICAN CHEMICAL SOCIETY
pubs.acs.org/JACS
Article

Air-Stable Membrane-Free Magnesium Redox Flow Batteries

Rajeev K. Gautam, Jack J. McGrath, Xiao Wang, and Jianbing Jimmy Jiang*

Cite This: https://doi.org/10.1021/jacs.4c10106

ABSTRACT: Membrane-free biphasic self-stratified batteries (MBSBs) utilizing aqueous/nonaqueous electrolyte systems have garnered significant attention owing to their flexible manufacturing and cost-effectiveness. In this study, we present an ultrastable high-voltage Mg MBSB based on an aqueous/nonaqueous electrolyte system. The engineered aqueous electrolyte had a wide electrochemical stability window of 3.24 V. The Mg metal anode features a Mg^{2+}-conductive protective coating. Two metal-free redox compounds, 2,2,6,6-tetramethylpiperdinyl oxy (**TEMPO**) and *N*-propyl phenothiazine (**C3-PTZ**), were used as catholytes. The Mg||**TEMPO** and Mg||**C3-PTZ** MBSBs exhibited high cell voltages of 2.07 and 2.12 V, respectively, and were studied under static, stirred, and flow conditions. The Mg MBSBs were initially evaluated at different catholyte concentrations (0.1, 0.3, and 0.5 M) under static conditions. Notably, the Mg||**TEMPO** (0.5 M) and Mg||**C3-PTZ** (0.5 M) static batteries maintained exceptional performances over 500 cycles at 8 mA/cm^2, with capacity retention rates of 97.84% and 98.87%, Coulombic efficiencies of 99.17% and 99.12%, and capacity utilization of 70.2% and 71.3%, respectively. Under stirred and flow conditions, the Mg||**TEMPO** (0.5 M) and Mg||**C3-PTZ** (0.5 M) batteries cycled 500 times at 12 mA/cm^2 demonstrated capacity retention rates of 99.82% and 99.88% (stirred), 93.58% and 92.16% (flow), respectively. Under flow conditions, the Mg||**TEMPO** (0.5 M) and Mg||**C3-PTZ** (0.5 M) batteries demonstrated power densities of 195 and 191 mW/cm^2, respectively, surpassing those of 139 and 144 mW/cm^2 under static conditions. These cost-effective Mg MBSBs exhibit remarkable performance and advance the application of Mg chemistry in organic flow batteries.

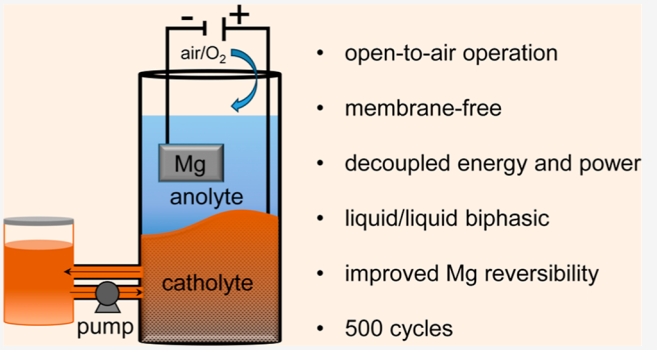

INTRODUCTION

The global pursuit of efficient and sustainable energy-storage solutions has driven significant advancements in battery technology.[1] With the ever-increasing demand for renewable energy sources, there is a pressing need for robust energy storage technologies that can buffer intermittent energy production and provide a reliable power supply.[2,3] Lithium-ion batteries have emerged as a dominant technology in various applications.[4] However, Li-ion batteries have several significant limitations, including limited material resources, high costs, and safety concerns.[4,5] These unresolved problems have prompted the development of new types of batteries that can offer higher energy density and better sustainability than Li-ion batteries. Potential alternatives to Li-ion batteries include alkaline earth metals (Mg^{2+}, Ca^{2+}), alkali metals (Na^+, K^+), group IIIA metals (Al^{3+}), and transition metals (Zn^{2+}).[6] Among the emerging alternatives, Mg-ion batteries have received significant attention owing to the abundance of Mg, the high theoretical volumetric capacity of Mg compared to that of Li (3833 vs 2046 mA h/cm^3), low cost, and environmental friendliness.[7,8] In addition, Mg metal demonstrates reduced dendrite formation during battery cycling, surpassing that of both Li and Zn, owing to its low diffusion barrier and unique planar hexagonal growth during electrochemical deposition.[8] Hence, Mg-ion batteries hold promise as a viable and sustainable energy storage technology capable of meeting escalating energy demands while mitigating environmental impacts. Recent advances in Mg-ion batteries have primarily focused on solid-state rechargeable batteries.[7,9] Despite the significant progress made in improving the performance of Mg-ion solid-state batteries, the development of Mg-based flow batteries is still in its early stages. Recent studies by Qin et al.[10] and He et al.[11] used polymer and polysulfides as catholytes, respectively. Unlike solid-state rechargeable batteries, Mg-based flow batteries offer independent scaling of energy and power as well as compatibility with diverse catholytes.[12] However, the implementation of Mg-based flow batteries faces significant obstacles, including (1) the limited availability and high cost of ion-exchange membranes in both aqueous and nonaqueous electrolyte systems,[13,14] and (2) the requirement for electrolyte systems

Received: July 24, 2024
Revised: September 25, 2024
Accepted: September 26, 2024

with highly reversible Mg chemistry.[15,16] The first issue can be addressed by using membrane-free biphasic self-stratified batteries (MBSBs). Different configurations of MBSBs have been designed,[17] and various redox chemistries have been explored by others[18−26] and our group.[27−30] An optimal biphasic system includes an anolyte with a highly reversible Mg anode and minimal solubility of the cathode materials. Simultaneously, the catholyte should exhibit high solubility and electrochemical stability. In general, liquid/liquid biphasic systems are divided into three categories based on the solvents used as the anolyte and catholyte: aqueous/aqueous,[18,31] aqueous/nonaqueous,[22−24,27] and nonaqueous/nonaqueous.[25,28,30] Before selecting a specific biphasic system to design a Mg-based MBSB system, it is imperative to thoroughly understand the electrochemical behavior of Mg metal within a particular type of electrolyte. The reversible chemistry of Mg metal anodes has been studied in both aqueous and nonaqueous electrolyte systems.

Notable nonaqueous electrolyte systems explored for Mg metal anodes include Grignard reagents/tetrahydrofuran[32] or dimethyl ether,[33] magnesium organoborate electrolytes, magnesium aluminum chloride complexes,[34−36] Mg hexamethyldisilazane,[37,38] and magnesium bis(trifluoromethanesulfonimide) ($Mg(TFSI)_2$)[39] (Figure 1). Although several of these systems effectively prevent passivation film growth or facilitate reversible Mg stripping/plating, the organic solvents often exhibit electrochemical oxidative instability and poor conductivity.[40] In addition, the use of highly volatile ethereal solvents and metal complexes may increase safety and cost concerns.[41] Ionic liquids (ILs) are a promising alternative because of their high electrochemical stability, low flammability, and high ionic conductivity;[42,43] however, the use of an IL as a neat electrolyte solvent is considerably expensive.[44,45]

In contrast to nonaqueous systems, aqueous solvents offer the advantages of high ionic conductivity, low cost, safe operation, and environmental friendliness. However, aqueous electrolytes present two significant challenges when applied to Mg-ion batteries. First, the tendency of Mg to form surface passivation layers composed of magnesium oxide (MgO) and magnesium hydroxide ($Mg(OH)_2$) when exposed to water is a major hurdle.[8] Second, the narrow electrochemical stability window (ESW) of water (1.23 V) imposes constraints on achieving a high cell voltage.[46] To address these challenges, extensive research efforts have focused on developing stable high-voltage aqueous electrolytes for Mg-ion batteries.[8,47,48] One promising approach involves the use of high-concentration Mg salts such as magnesium chloride ($MgCl_2$) or $Mg(TFSI)_2$,[30,47] aiming at reducing the free water content, thus mitigating Mg surface passivation.[8,47] Another approach involves the use of solvent additives to enhance the ESW of aqueous electrolytes.[48] These strategies facilitate the direct utilization of Mg metal in aqueous electrolytes, thereby improving the kinetics of Mg-ion batteries. In addition, the immiscibility of water with various nonaqueous solvents, whether in their neat form or through a salt-out strategy, facilitates the rapid formation of stable aqueous/nonaqueous biphasic self-stratified systems. These systems are well-suited for the development of liquid/liquid membrane-free redox flow batteries (RFBs).

In this study, we developed a membrane-free biphasic system based on aqueous/nonaqueous electrolytes (Figure S1). The aqueous electrolyte, strategically modified with

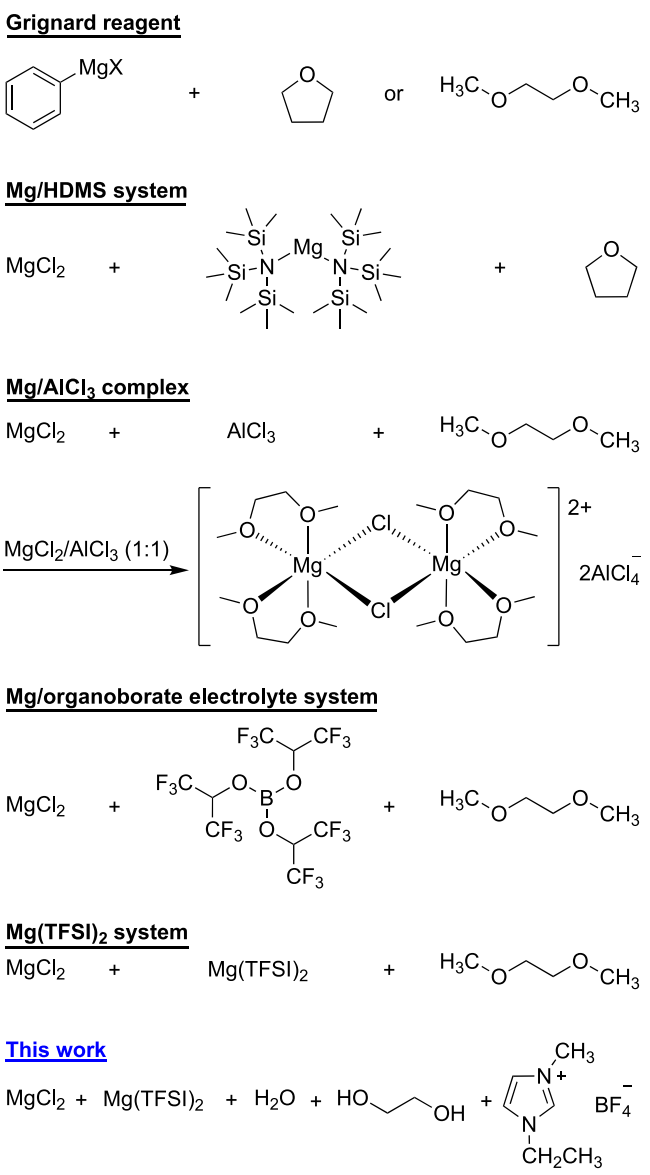

Figure 1. Reported electrolyte systems for Mg-ion batteries.

solvent additives, including ethylene glycol (EG) and an IL, was paired with Mg metal serving as the anolyte. Dichloromethane (CH_2Cl_2) with the organic redox compounds (2,2,6,6-tetramethylpiperidinyl-1-yl)oxyl (**TEMPO**) and *N*-propyl phenothiazine (**C3-PTZ**) served as catholyte. The developed anolyte was positioned on top of the catholyte, forming Mg||**TEMPO** and Mg||**C3-PTZ** MBSBs with operational voltages of 2.07 and 2.12 V, respectively. To prevent Mg metal passivation and enhance its reversible chemistry within the developed aqueous anolyte, we designed a Mg metal anode with an effective Mg^{2+}-conductive polymer coating. Subsequently, the Mg||**TEMPO** and Mg||**C3-PTZ** MBSBs were evaluated over long-term charge/discharge cycles under static, stirred, and flowing catholyte conditions. The newly developed cost-effective Mg MBSBs exhibited remarkable performance, thus paving the way for innovative applications of Mg chemistry in organic flow batteries.

https://doi.org/10.1021/jacs.4c10106
J. Am. Chem. Soc. XXXX, XXX, XXX−XXX

RESULT AND DISCUSSION

Designing of Electrolyte Systems. Water was used as the anolyte solvent to fabricate the biphasic system. However, the narrow ESW of water restricts the development of batteries with cell voltages greater than 1.2 V.[47,49] Therefore, widening the ESW range of aqueous electrolyte systems is crucial to enable their use in Mg-based batteries. Various strategies, including the use of water-in-salt and solvent additives, have been widely explored for different battery applications.[8,46−49] In the water-in-salt strategy, higher concentrations of electrolyte salts are introduced into the aqueous electrolytes to extend their ESW limits. The choice of salt is crucial, and it should exhibit a high solubility in water and be electrochemically compatible with the redox materials. Therefore, to design an aqueous anolyte for the Mg MBSB system, two Mg-based salts, $MgCl_2$ and $Mg(TFSI)_2$, were specifically selected because of extensive studies on Mg-ion battery research.[8,33,50] The water/$MgCl_2$ (1 M) electrolyte system demonstrated an ESW of approximately 1.53 V (Figure 2).

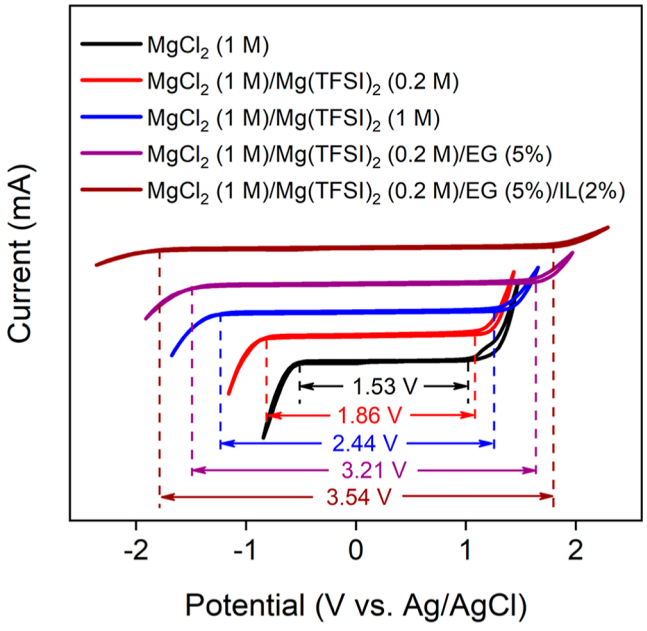

Figure 2. ESW of water with different concentrations of Mg salt and solvent additives.

To further increase the ESW, different concentrations (0.2 and 1 M) of $Mg(TFSI)_2$ were added to the water/$MgCl_2$ (1 M) electrolyte. The addition of both concentrations of $Mg(TFSI)_2$ broadened the ESW of the water/$MgCl_2$ (1 M) electrolyte, with the water/$MgCl_2$ electrolyte with 1 M $Mg(TFSI)_2$ exhibiting a slightly higher ESW. However, the use of a higher concentration of $Mg(TFSI)_2$ may increase the overall cost of the battery system. Therefore, a lower concentration of $Mg(TFSI)_2$ (0.2 M) in the water/$MgCl_2$ (1 M) electrolyte was used for further electrochemical improvement.

The use of solvent additives is another widely explored strategy for enhancing the ESW of electrolytes.[46] Solvents such as ILs,[51] poly(ethylene) glycol (PEG),[52] and EG[53] have been explored as promising additives for extending the ESW of aqueous electrolytes. Therefore, EG and an IL (1-ethyl-3-methylimidazolium tetrafluoroborate) were selected as the solvent additive for aqueous electrolytes. The ability of EG to create stable complexes with magnesium ions,[54] combined with the wider ESW and high chemical stability of the IL (Figure S2), potentially contributes to a broader ESW for aqueous electrolytes. The combination of EG and IL provided an optimal electrolyte composition that could further extend the ESW of the developed aqueous electrolyte (Figure 2). Hence, EG (5%) and IL (2%) were added to the developed electrolyte system, resulting in the formation of a water/$MgCl_2$ (1 M)/$Mg(TFSI)_2$ (0.2 M)/EG (5%)/IL (2%) electrolyte with an ESW of 3.53 V (Figure 2). The electrolyte salt potassium hexafluorophosphate (KPF_6) (0.25 M) was also added to the aqueous electrolyte to provide PF_6^- as an exchange charge carrier in the biphasic system. This final aqueous electrolyte system, water/$MgCl_2$ (1 M)/$Mg(TFSI)_2$ (0.2 M)/KPF_6 (0.25 M)/EG (5%)/IL (2%), labeled WEIL, was employed in all subsequent experiments.

Dichloromethane (CH_2Cl_2) was selected as a cathode solvent for various reasons. First, the high solubilizing ability of CH_2Cl_2 allows the screening of a wide range of redox-active compounds. Second, the immiscibility of CH_2Cl_2 with water facilitated the formation of self-stratified biphasic systems. Third, the density of CH_2Cl_2 is higher than that of water, maintaining the CH_2Cl_2 electrolyte at the bottom layer of the biphasic system to avoid direct air exposure of the catholyte. In addition, the use of CH_2Cl_2 as the catholyte solvent was successfully demonstrated in our previous study.[27] Tetrabutylammonium hexafluorophosphate ($TBAPF_6$) (1.5 M) was used as the electrolyte salt, which provided PF_6^- as an exchange charge carrier in the biphasic system.

Design of the Mg Metal Anode with Mg^{2+} Conductive Polymer Interface. Reversible Mg chemistry is crucial for the high and efficient performance of Mg RFB systems. In the developed electrolyte system, the use of solvent additives facilitated higher Mg reversible performance (Figure S3). However, Mg metal is still exposed to water molecules and exhibits a high tendency to form surface passivation layers. To mitigate this issue of passivation layer formation, high concentrations of salt in water have been explored to decrease the water content and prevent passivation of the Mg metal anode.[8]

Another strategy involves the application of polymer coatings, which are effective in protecting Li and Zn metal anodes from dendrite formation.[55,56] The polymer coating establishes an ion-conducting interface between the electrolyte and metal, effectively suppressing dendrite growth by preventing direct contact between the metal and electrolyte. Motivated by this approach, we developed a modified Mg metal anode featuring a protective polymer layer that facilitates Mg^{2+} conduction from the electrolyte to the electrode surface. This strategy avoids direct contact between the Mg metal and water molecules, thereby significantly mitigating the passivation of the Mg metal surface. To prepare the surface-modified Mg metal anode, poly(vinylidene fluoride-*co*-hexafluoropropylene) (PVDF-HFP), $Mg(TFSI)_2$, and $Mg(OTf)_2$ at a 2:1:1 mass ratio were magnetically stirred in *N*,*N*-dimethylformamide for 24 h to generate a clear polymer solution. The polymer solution was then coated onto the Mg metal surface via a dip-coating process. Following each coating, the polymer on the Mg metal surface was thermally heated before the subsequent coat was applied. This procedure was repeated for a total of eight coatings. Two additional Mg samples, PVDF-HFP/$Mg(TFSI)_2$ (2:1 mass ratio) and PVDF-HFP/$Mg(OTf)_2$

https://doi.org/10.1021/jacs.4c10106
J. Am. Chem. Soc. XXXX, XXX, XXX−XXX

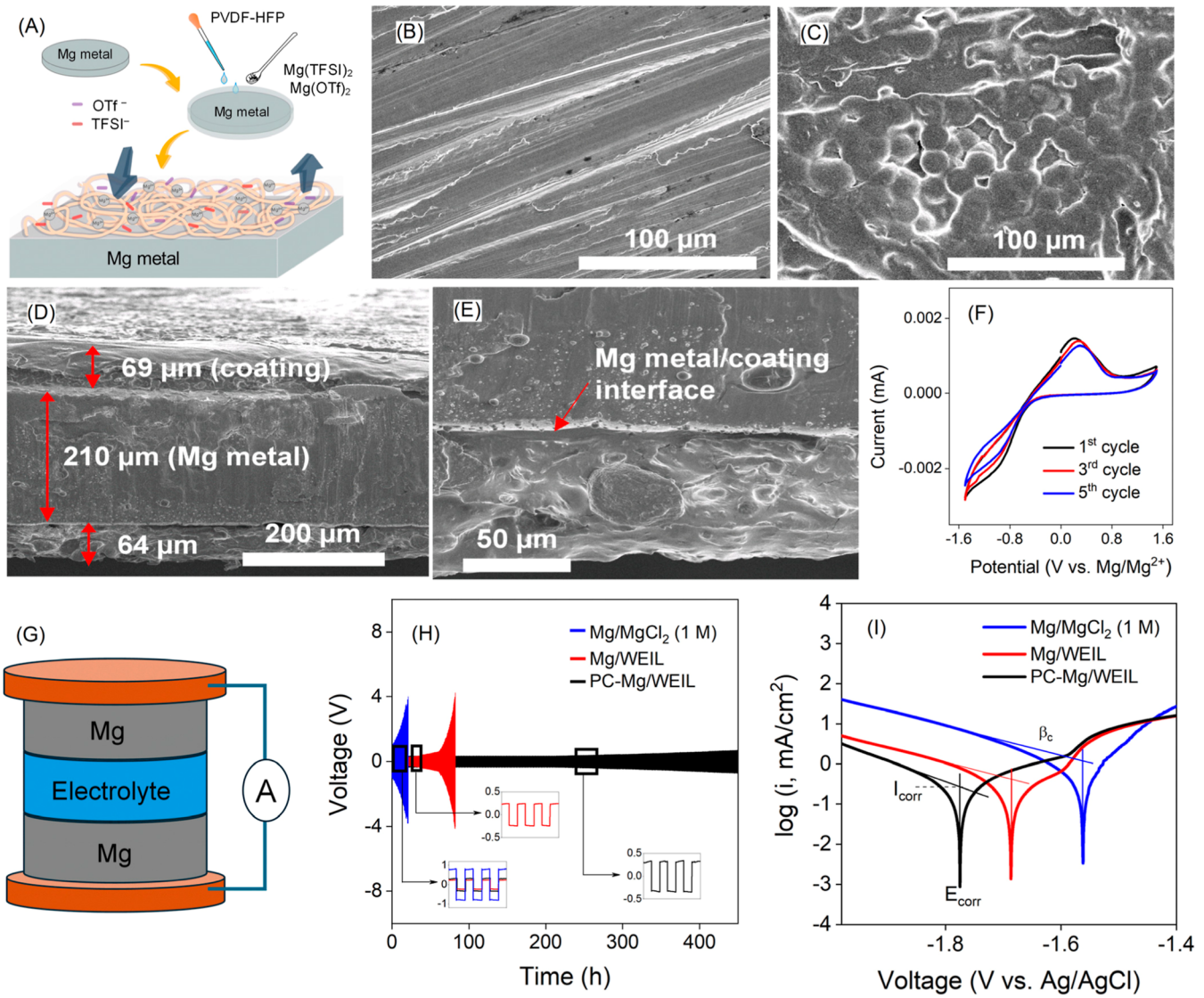

Figure 3. (A) Schematic showing the preparation and microstructure of the surface-modified Mg metal anode. Surface morphologies of the (B) bare and (C) surface modified Mg metal anodes. (D) Surface morphology showing the thickness of the Mg metal anode and polymer coating. (E) Magnified surface morphology showing metal/coating interface. (F) Electrochemical reversibility of the PVDF-HFP/$Mg(TFSI)_2$/$Mg(OTf)_2$ modified Mg metal anode in the developed aqueous electrolyte (WEIL). (G) Schematic of the Mg||Mg symmetrical cell. (H) Cycling stabilities of the bare Mg||Mg symmetrical cell in 1 M $MgCl_2$ electrolyte, bare Mg||Mg symmetrical cell in WEIL electrolyte, and PC-Mg||PC-Mg symmetrical cell in WEIL electrolyte. (I) Tafel polarization curves of bare Mg in bare 1 M $MgCl_2$ electrolyte, bare Mg in WEIL electrolyte, and PC-Mg in WEIL electrolyte.

(2:1 mass ratio) were prepared using the same method and used for the control experiments. All the processes were conducted in an argon-filled glovebox (moisture level <1.0 ppm). A schematic of the preparation of the modified Mg metal anode is shown in Figure 3A. The surface morphologies of the bare and polymer-coated Mg metal anodes are illustrated in Figure 3B,C, respectively, indicating that the polymer coating was uniform on the Mg metal surface. The metal anode has a uniform coating of Mg^{2+}-conductive polymer with an average thickness of approximately 65 μm (Figure 3DE). Moreover, energy-dispersive X-ray mapping (Figure S4) revealed that the salt in the polymer coating was uniformly distributed. Electrochemical analyses (Cyclic voltammetry (CV) arrangement shown in Figure S5) revealed that the Mg metal anodes modified with PVDF-HFP/$Mg(OTf)_2$ (Figure S6) or PVDF-HFP/$Mg(TFSI)_2$ (Figure S7) exhibited inferior Mg reversibility compared to those of PVDF-HFP/$Mg(TFSI)_2$/$Mg(OTf)_2$ (Figure 3F). The improved Mg reversibility of the PVDF-HFP/$Mg(TFSI)_2$/$Mg(OTf)_2$ modified Mg metal anode is attributed to the better oxidative and high ion mobility behavior of the combination of the $Mg(OTf)_2$ and $Mg(TFSI)_2$ salts.[57−59] Overall, the polymer-coated Mg metal anode with an efficient Mg^{2+}-conductive interface minimized the direct contact between Mg and the electrolyte. This protected Mg from passivation by preventing electrolyte reduction on the Mg surface, thereby offering high Mg reversibility. To assess the performance improvements provided by the WEIL and the conducting polymer coating on the Mg metal anode (PC-Mg), we examined the cycling stability of Mg||Mg and PC-Mg||PC-Mg symmetrical cells (Figure 3G). The Mg||Mg symmetrical cell with a 1 M $MgCl_2$ electrolyte exhibited significant polarization after 22 h of cycling (Figure 3H), indicating that the Mg stripping/plating process in 1 M $MgCl_2$ is

https://doi.org/10.1021/jacs.4c10106
J. Am. Chem. Soc. XXXX, XXX, XXX−XXX

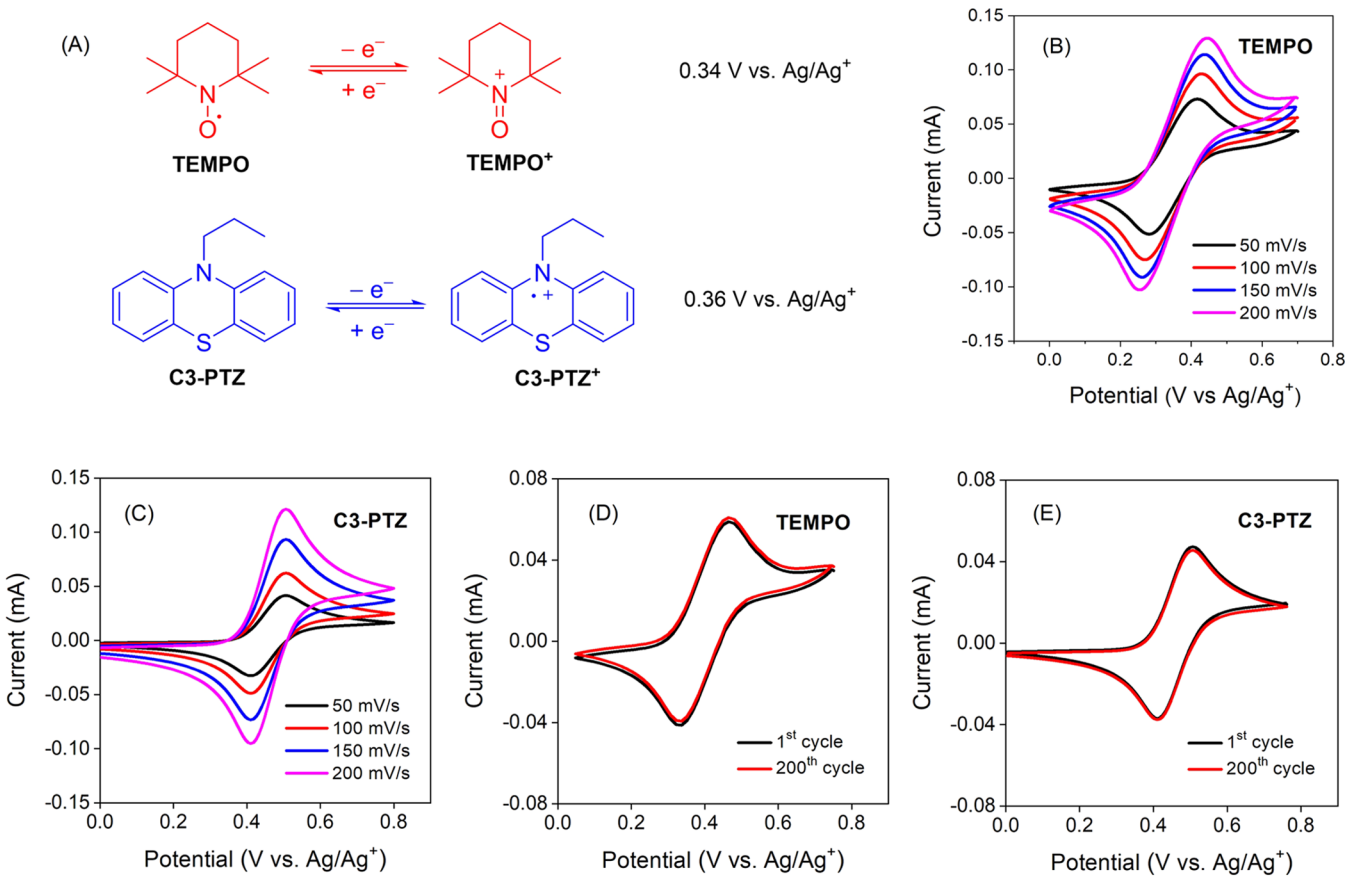

Figure 4. (A) Chemical structures and redox voltages of **TEMPO** and **C3-PTZ**. Cyclic voltammograms of (B) **TEMPO** and (C) **C3-PTZ** in CH_2Cl_2/TBAPF$_6$ (0.1 M) at various scan rates from 50 to 200 mV/s. CV cycling stability of (D) **TEMPO** and (E) **C3-PTZ** for 200 cycles.

unsustainable because of severe surface corrosion induced by extensive hydrogen evolution reactions (HERs). In contrast, the modified electrolyte system significantly enhanced the Mg stability for 82 h (182 cycles) compared to the 1 M $MgCl_2$ electrolyte system. However, the modified electrolyte system (WEIL) cannot completely prevent Mg surface oxidation. Hence, further improvements are essential for enhancing the stability of Mg. The cycling stability of the surface-modified PC-Mg||PC-Mg in the WEIL electrolyte was maintained for 450 h (1000 cycles). The Mg^{2+}-conductive polymer layer in the PC-Mg anode significantly reduced surface corrosion by preventing direct contact of water molecules with the Mg surface, thereby providing stable stripping/plating behavior. To further confirm the capability of the developed electrolyte to facilitate reversible Mg chemistry, we performed electrochemical plating of Mg onto Cu at a reduction potential of −1.5 V vs Ag/AgCl for different time durations of 20, 40, and 60 min. After electrodeposition, the vacuum-dried samples were characterized using scanning electron microscopy (SEM), energy-dispersive X-ray spectroscopy (EDX), and X-ray diffraction (XRD) techniques. SEM analysis (Figure 8) reveals the presence of electrodeposited material on bare Cu (Figure S8A) at all durations (Figure S8B−D). EDX analysis confirms the deposition of Mg along with other elements (Figure S9). The EDX spectra (Figure S9A) and elemental mapping (Figure S9B−J) show the relative distribution of Cu and Mg, as well as C, F, O, S, and Cl. In addition, XRD analysis (Figure S10) supports the presence of Mg deposition. These results demonstrate that the developed electrolyte effectively facilitates reversible Mg chemistry for the polymer-coated Mg metal anode. Moreover, corrosion experiments (Figure 3I), revealed that the PC-Mg/WEIL electrolyte reduced the corrosion current (i_{corr}) from 1.58 to 0.45 mA compared to that of the Mg/$MgCl_2$ (1 M) electrolyte, indicating a slower corrosion rate due to surface oxidation of the PC-Mg metal anode. Moreover, the βc value, which indicates the strength of HERs,[8] was reduced for the PC-Mg/WEIL system (297 mV/dec) compared to that of the bare Mg/$MgCl_2$ metal anode (373 mV/dec). Hence, the PC-Mg/WEIL system significantly suppressed both surface corrosion and HERs.

Selection of the Redox-Active Cathode Materials. Rational selection of the redox-active cathode materials for a biphasic system is of utmost importance. To minimize crossover, the cathode materials should exhibit high solubility in the catholyte solvent and minimal solubility in the anolyte. To identify catholyte materials meeting the solubility criteria, 11 redox-active compounds, including derivatives of phenothiazine (**C3-PTZ**), cyclopropenium (CP), **TEMPO**, and tetrathiafulvalene (PEG3-TTF) were tested for their solubilities in both phases of the biphasic system (Table S1). Among these 11 compounds, **TEMPO** and **C3-PTZ** (Figure 4A) exhibited excellent solubility in the CH_2Cl_2 electrolyte and negligible solubility in the anolyte. Consequently, **TEMPO** and **C3-PTZ** were used as cathode materials in subsequent electrochemical and battery cycling studies.

Electrochemical Characterization. CV analysis was employed to investigate the electrochemical properties of the cathode materials (Figure 4A) in a CH_2Cl_2/TBAPF$_6$ (0.1 M)

https://doi.org/10.1021/jacs.4c10106
J. Am. Chem. Soc. XXXX, XXX, XXX−XXX

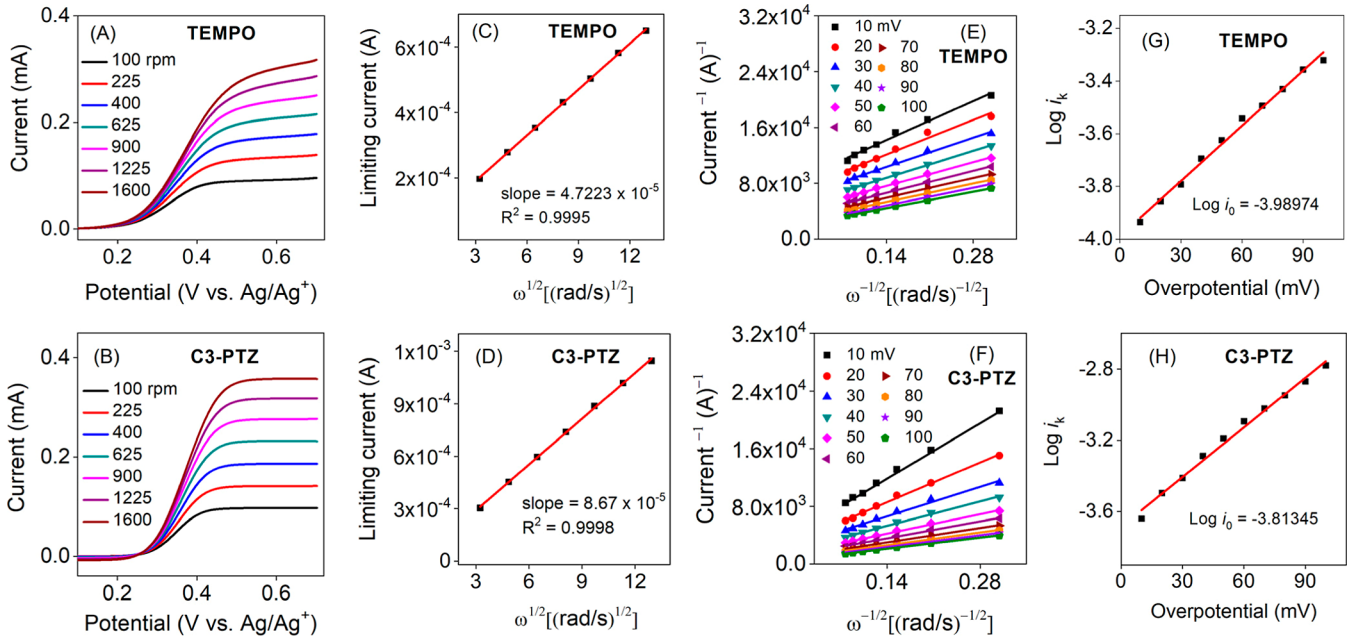

Figure 5. LSV curves of (A) **TEMPO** and (B) **C3-PTZ** at a scan rate of 5 mV/s and rotation rates from 100 to 1600 rpm. Fitted linear Lévich plots of the limiting current (i_L) vs the square root of rotation rates ($\omega^{1/2}$) of (C) **TEMPO** and (D) **C3-PTZ**. Linearly fitted Koutecký−Lévich plots of i^{-1} vs $\omega^{-1/2}$ for (E) **TEMPO** and (F) **C3-PTZ**. Linearly fitted plots of log i_k as a function of overpotential for (G) **TEMPO** and (H) **C3-PTZ**. The rotating disc electrode experiments were performed with 1 mM redox materials in CH_2Cl_2/$TBAPF_6$ (0.1 M).

electrolyte. Both **TEMPO** and **C3-PTZ** displayed reversible redox couples at 0.34 and 0.36 V vs Ag/Ag^+, respectively, with a peak separation of 71 and 76 mV at a scan rate of 50 mV/s (Figure 4B,C), indicating a one-electron redox process as per the Nernst equation.[60] In addition, CV measurements were conducted at various rates ranging from 50 to 200 mV/s (Figure 4B,C) to study the electrochemical kinetics of the catholyte compounds. The ratios of the cathodic peak current (i_{pc}) to the anodic peak current (i_{pa}) of **TEMPO** and **C3-PTZ** were close to 1 at the investigated scan rates (Figure S11A,B), suggesting excellent electrochemical reversibility in the CH_2Cl_2 electrolyte. Moreover, the anodic and cathodic currents exhibited a linear relationship with the square root of the scan rate ($\nu^{1/2}$) for both **TEMPO** and **C3-PTZ** (Figure S12A,B), indicating that the redox process is diffusion-controlled.[60] In addition to their remarkable electrochemical reversibility, based on repeated CV scans (Figure 4D,E), both **TEMPO** and **C3-PTZ** displayed high electrochemical stability in the catholyte. The molecules were also studied using linear sweep voltammetry (LSV) with a rotating disk electrode (Figure 5).

The diffusion coefficient of the redox-active cathode materials dictates ion movement during charging and discharging, impacting the overall electrochemical performance; therefore, characterizing the diffusion coefficient is essential for optimizing battery design and enhancing energy storage capabilities. The electrochemical kinetics of the catholyte. The rotation rates (ω) varied from 100 to 1600 rpm, which revealed distinct plateaus in the mass-transport-controlled limiting currents (i_L) (Figure 5A,B). The Koutecký−Lévich curves (Figure 5C,D) represent linear correlations between i_L and the square root of the rotation rate ($\omega^{1/2}$) for both **TEMPO** and **C3-PTZ**. From the slopes of the fitted linear Lévich plots (Figure 5C,D), the diffusion coefficients (D) for **TEMPO** and **C3-PTZ** were determined to be 4.78 × 10^{-6} and 4.86 × 10^{-6} cm^2 s^{-1}, respectively. The electrochemical kinetic rate constants for the charge-transfer reactions of the cathodic redox materials were obtained using the Koutecký−Lévich eq (eq S2) (Figure 5E,F). The linear correlations between i^{-1} and $\omega^{-1/2}$ for **TEMPO** and **C3-PTZ** at different overpotentials (η = 10 to 100 mV) were used to estimate the i_k values, which are plotted as a function of the overpotential in Figure 5G,H. The kinetic rate constants (k_0) of **TEMPO** and **C3-PTZ** were calculated to be 3.23 × 10^{-3} and 3.21 × 10^{-3} cm s^{-1}, respectively, using eq S2. Remarkably, the diffusion coefficients and rate constants of the catholyte materials are comparable to those of redox-active organic materials commonly used in aqueous flow batteries.[61,62] The 9,10-anthraquinone-2,7-disulfonic acid[61] and hydroquinone[62] exhibit a diffusion coefficient on the order of 10^{-6} cm^2 s^{-1} and a kinetic reduction rate constant of 10^{-3} cm s^{-1}, which is comparable to the diffusion coefficient and rate constant of **TEMPO** and **C3-PTZ** used in this system.

Battery Cycling Performance under Static Conditions. The cycling performances of the membrane-free batteries were first examined under static conditions in terms of capacity retention, voltage profiles, and Coulombic, voltage, and energy efficiencies. All the charge/discharge experiments were performed with exposure to air under ambient conditions. As a starting point, the Mg metal anode was paired with **TEMPO** and **C3-PTZ** redox-active catholytes at concentrations of 0.1 and 0.3 M, resulting in the formation of Mg|| **TEMPO** and Mg||**C3-PTZ** MBSBs.

Battery Cycling Performance under Static Conditions. The cycling performances of the membrane-free batteries were first examined under static conditions in terms of capacity retention, voltage profiles, and Coulombic, voltage, and energy efficiencies. All the charge/discharge experiments were performed with exposure to air under ambient conditions. As a starting point, the Mg metal anode was paired with **TEMPO** and **C3-PTZ** redox-active catholytes at concentrations of 0.1 and 0.3 M, resulting in the formation of Mg||

https://doi.org/10.1021/jacs.4c10106
J. Am. Chem. Soc. XXXX, XXX, XXX−XXX

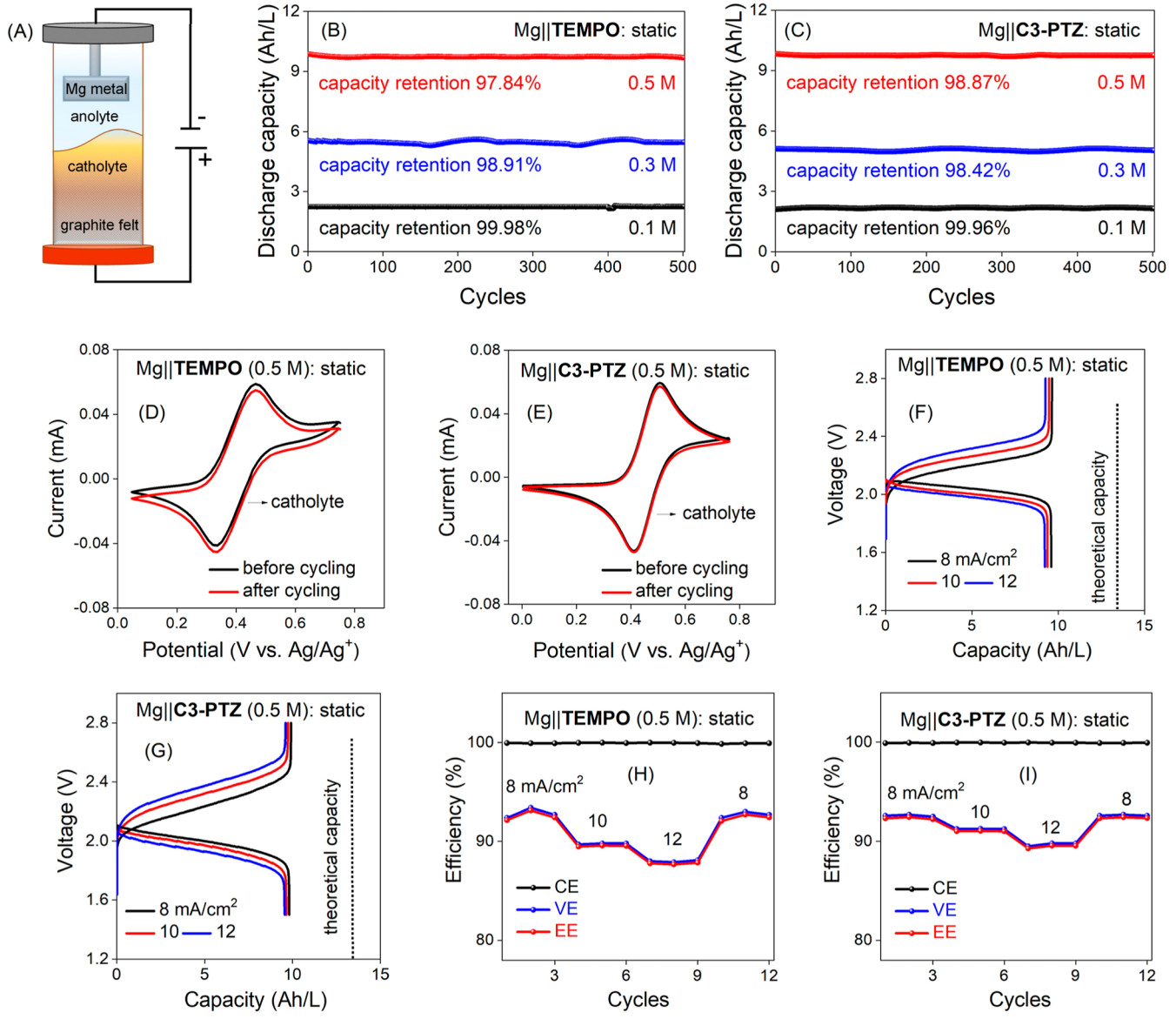

Figure 6. Long-term charge/discharge performance of Mg||**TEMPO** (0.5 M) and Mg||**C3-PTZ** (0.5 M) batteries under static conditions. (A) Schematic of the Mg-based MBSB static battery. Capacity retention and efficiency evaluation of (B) Mg||**TEMPO** (0.5 M) and (C) Mg||**C3-PTZ** (0.5 M) at a current density of 8 mA/cm^2. CV curves of (D) Mg||**TEMPO** (0.5 M) and (E) Mg||**C3-PTZ** (0.5 M) before and after long-term battery cycling. Charge/discharge profiles of (F) Mg||**TEMPO** (0.5 M) and (G) Mg||**C3-PTZ** (0.5 M) at different current densities. Variation in the CE, VE, and energy efficiency (EE) of (H) Mg||**TEMPO** (0.5 M) and (I) Mg||**C3-PTZ** at different current densities.

TEMPO and Mg||**C3-PTZ** MBSBs. Subsequently, both the batteries were charged and discharged for 500 cycles at a current density of 8 mA/cm^2. A schematic and digital photograph of the static battery setup are shown in Figures 6A and S13, respectively. Notably, the operational current density exceeded those previously reported for aqueous/nonaqueous (~5 mA/cm^2)[22−24,27,29] and nonaqueous/nonaqueous (~2 mA/cm^2)[25,28,30] MBSBs (Table S1). The Mg||**TEMPO** (0.1 M) and Mg||**C3-PTZ** (0.1 M) batteries exhibited theoretical capacity utilizations of 76.9% and 77.4%, respectively, capacity retentions of 99.98% (99.999 per cycle, 99.998 per day) (~15 days) and 99.96% (99.999 per cycle, 99.998 per day) (~18 days) (Figure 6B,C), Coulombic efficiencies (CE) of 99.63% and 99.43%, voltage efficiencies (VE) of 91.24% and 92.15%, and energy efficiencies (EE) of 90.56% and 91.31% (Figure S14A,B). In contrast, the Mg||**TEMPO** (0.3 M) and Mg||**C3-PTZ** (0.3 M) batteries exhibit capacity utilization of 71.6% and 72.3%, respectively, capacity retentions of 98.91% (99.997 per cycle, 99.974 per day) (~41 days) and 98.42% (99.996 per cycle, 99.965 per day) (~45 days) (Figure 6B,C), CE of 99.17% and 99.21%, VE of 91.16% and 91.21%, and EE of 90.41% and 91.52% (Figure S15A,B). All Mg||**TEMPO** (0.1 and 0.3 M) and Mg||**C3-PTZ** (0.1 and 0.3 M) batteries exhibit high-capacity retentions and CE, confirming the high stability of redox-active materials. Moreover, the high cycling performances of both MBSBs highlight the high reversibility of the Mg metal anode in the developed aqueous anolyte system. To further enhance the energy density, we developed Mg||**TEMPO** and Mg||**C3-PTZ** MBSBs with higher concentrations of redox-active materials (0.5 M). Both batteries were tested for their long-term charge/discharge performance over 500 cycles. Mg||**TEMPO** (0.5 M) and Mg||**C3-PTZ** (0.5 M) demonstrated good capacity utilizations of 70.2% and 71.3%, respectively, capacity

https://doi.org/10.1021/jacs.4c10106
J. Am. Chem. Soc. XXXX, XXX, XXX−XXX

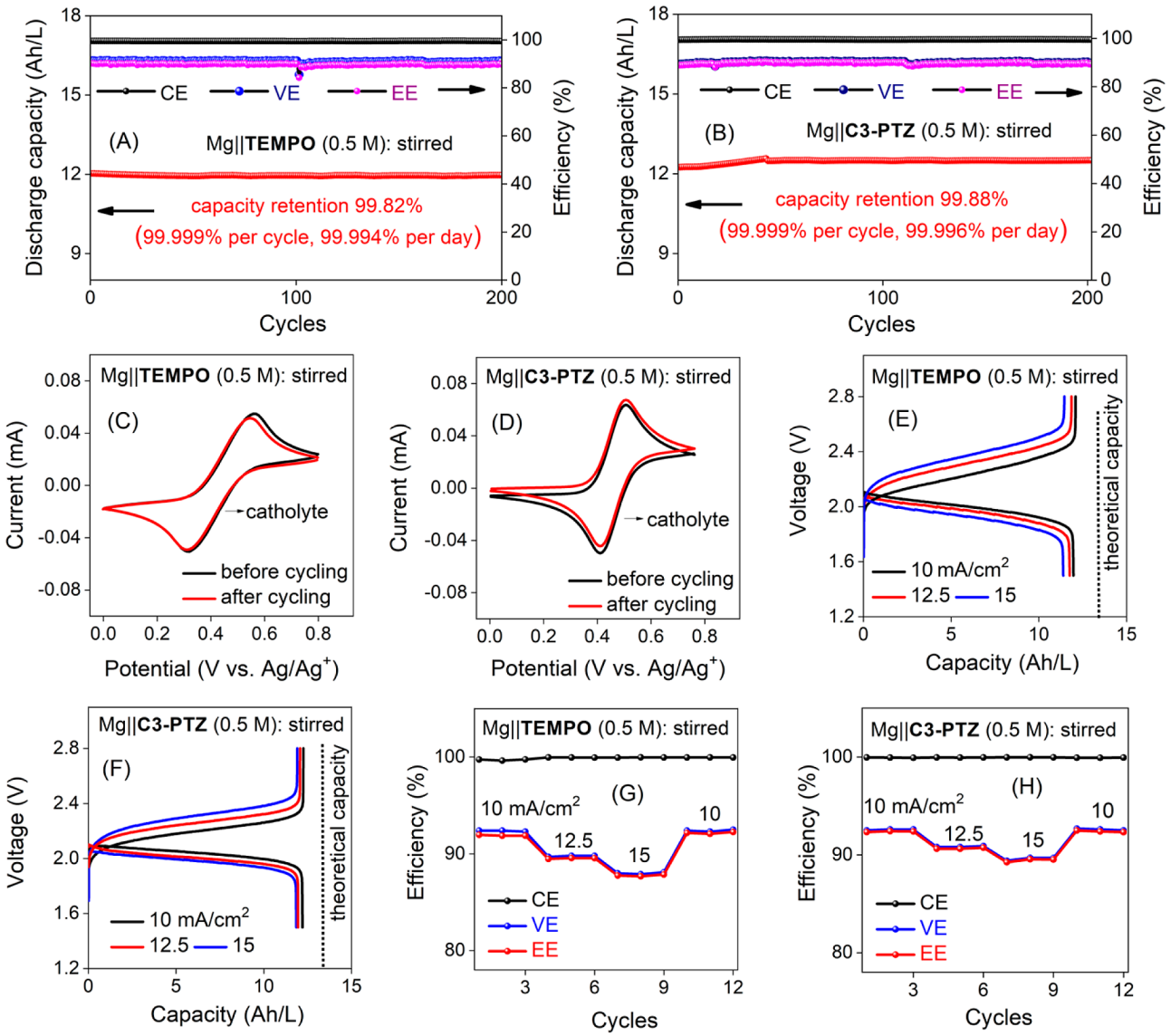

Figure 7. Long-term charge/discharge performance of Mg||**TEMPO** (0.5 M) and Mg||**C3-PTZ** (0.5 M) MBSBs under stirred conditions. Capacity retention and efficiency of (A) Mg||**TEMPO** (0.5 M) and (B) Mg||**C3-PTZ**. Both batteries were operated at a charge/discharge current density of 10 mA/cm^2. CV curves of (C) Mg||**TEMPO** (0.5 M) and (D) Mg||**C3-PTZ** (0.5 M) catholytes before and after long-term battery cycling. Charge/discharge profiles of (E) Mg||**TEMPO** (0.5 M) and (F) Mg||**C3-PTZ** (0.5 M) at different current densities. Variation in CE, VE, and energy efficiency (EE) of (G) Mg||**TEMPO** (0.5 M) and (H) Mg||**C3-PTZ** at different current densities.

retentions of 97.84% (99.997 per cycle, 99.975 per day) (~73 days) and 98.87% (99.997 per cycle, 99.975 per day) (~79 days) (Figure 6B,C), CE of 99.17% and 99.12%, VE of 91.52% and 91.61%, and EE of 91.76% and 90.81% (Figure S16A,B). Furthermore, the negligible change in the CV current intensity between the pre- and postcycled Mg||**TEMPO** (0.5 M) and Mg||**C3-PTZ** (0.5 M) MBSBs catholytes (Figure 6D,E) and anolytes (Figure S17A,B) implies the high electrochemical stability of the redox-active materials as well as the absence of crossover of these materials across the liquid/liquid interface throughout charge/discharge cycling.

In addition, both batteries displayed good self-discharging behavior over 170 h (~7 d) (Figure S18A,B). Low voltage drops over time (0.22 mV/h and 4.3 mV/day for Mg||**TEMPO** (0.5 M) and 0.24 mV/h and 5.7 mV/day for Mg||**C3-PTZ** (0.5 M)). Moreover, electrochemical impedance spectroscopy (EIS) analysis (Figure S19A,B) of the pre- and postcycled batteries revealed a negligible change in charge transfer resistance (R_{ct}), confirming the stable performance of the battery components, including the Mg metal anode and graphite felt, whereas a stable solution resistance (R_s) indicated the high stability of the electrolytes. Therefore, the observations from the CV and EIS analyses support the stable performance of both the Mg-based MBSBs. Also, the polymer matrix effectively maintains its structural integrity throughout the testing period (Figure S20). In addition to assessing the long-term charge/discharge performance, understanding the charge rate behavior of Mg-based MBSBs is essential for optimizing their performance. This ensures efficient energy storage, prolongs battery life, and enhances safety in practical deployment scenarios.

Therefore, to investigate the charge rate behavior, both the Mg||**TEMPO** (0.5 M) and Mg||**C3-PTZ** (0.5 M) MBSBs were subjected to charging/discharging under static conditions at current densities of 8, 10, and 12 mA/cm^2. With increasing current density, both batteries exhibited increased over-

https://doi.org/10.1021/jacs.4c10106
J. Am. Chem. Soc. XXXX, XXX, XXX−XXX

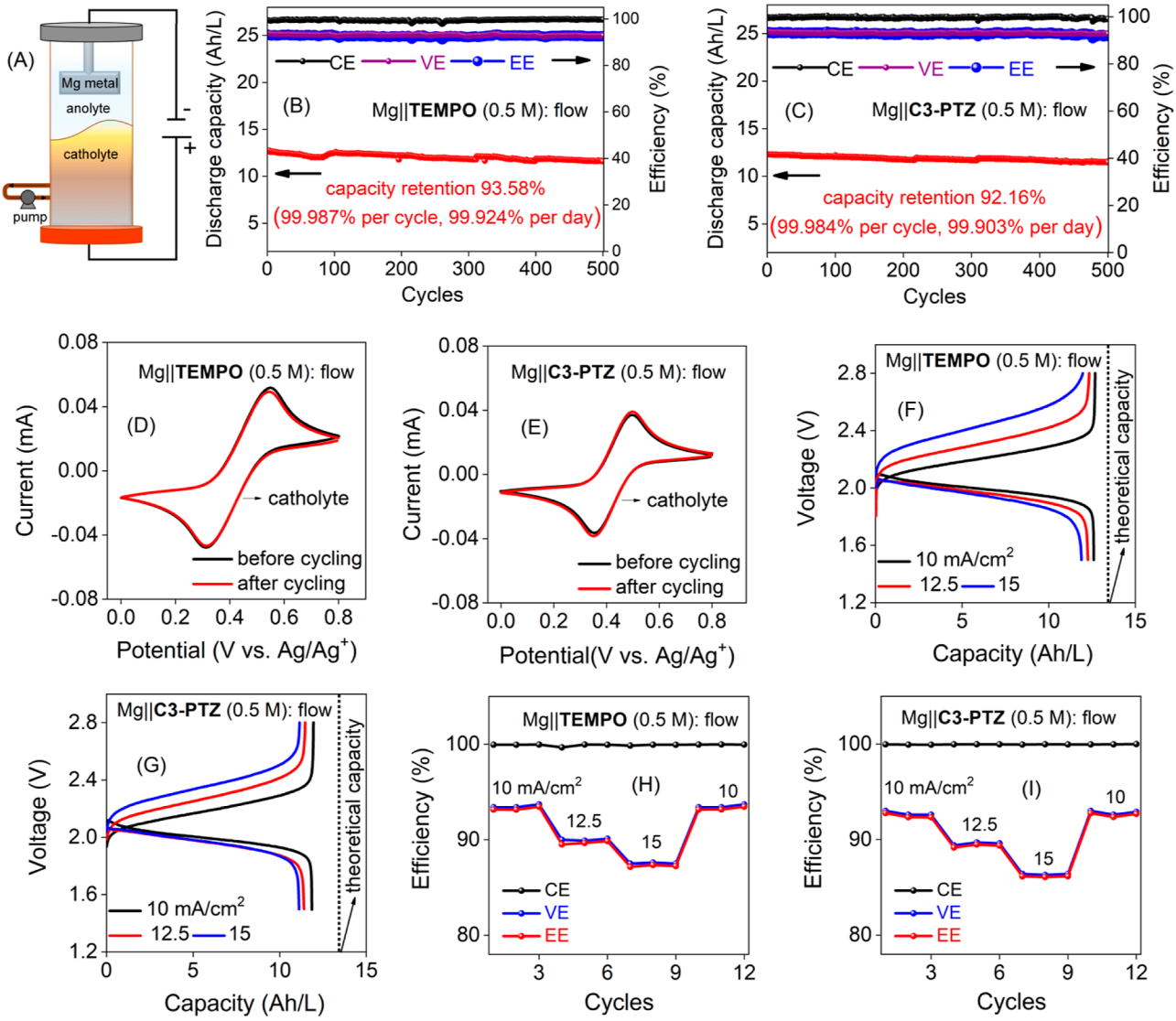

Figure 8. Long-term charge/discharge performance of Mg||**TEMPO** (0.5 M) and Mg||**C3-PTZ** (0.5 M) MBSBs under flow conditions. (A) Schematic of the Mg-based BSMB flow battery. Capacity retention and efficiency of (B) Mg||**TEMPO** (0.5 M) and (C) Mg||**C3-PTZ** (0.5 M) at a current density of 10 mA/cm^2. CV curves of (D) Mg||**TEMPO** (0.5 M) and (E) Mg||**C3-PTZ** (0.5 M) catholytes before and after long-term battery cycling. Charge/discharge profiles of (F) Mg||**TEMPO** (0.5 M) and (G) Mg||**C3-PTZ** (0.5 M) at different current densities. Variation in the CE, VE, and EE of (H) Mg||**TEMPO** (0.5 M) and (I) Mg||**C3-PTZ** at different current densities.

potentials during charging and discharging (Figure 6F,G), which was attributed to the mass diffusion limitation. Both the Mg||**TEMPO** (0.5 M) and Mg||**C3-PTZ** (0.5 M) batteries exhibited consistently high CE of ∼99.23% and ∼99.34%, respectively, at all operating current densities. This suggests that minimal side reactions occur during fast charging/discharging (Figure 6H,I). However, there was a notable decrease in their EE, from 91.52% to 87.21% for Mg||**TEMPO** (0.5 M) and from 92.12% to 88.33% for Mg||**C3-PTZ** (0.5 M). This decrease was attributed to an increase in the overpotential caused by mass-transport losses. Importantly, both the Mg-based MBSBs regained their original efficiencies when cycled back at 8 mA/cm^2, confirming their high charge-rate performance. Because mass-transport limitations affect energy delivery, monitoring the evolution of power density is crucial for improving battery efficiency and practicality. Therefore, power density analyses of the Mg||**TEMPO** (0.5) and Mg||**C3-PTZ** (0.5) static MBSBs were performed at different states of charge (SOCs). At a SOC of 100%, the peak power densities of the Mg||**TEMPO** (0.5 M) and Mg||**C3-PTZ** (0.5 M) batteries were 139 and 144 mW/cm^2, respectively (Figure S21A,B). In addition, the area-specific resistance (ASR) values were investigated for both the electrolyte and the entire cell (Figure S21C,D). Notably, the ASR decreased with increasing SOC, with the electrolyte resistance contributing ∼70% and ∼72% of the overall cell resistance of Mg||**TEMPO** (0.5 M) and Mg||**C3-PTZ** (0.5 M), respectively. These low ASR values enable batteries to operate even at a high current density of 12 mA/cm^2, as compared to previously reported membrane-free battery systems (Table S2).[22−25,27−30]

Battery Cycling Performance under Stirring and Flow Conditions. Although the static batteries demonstrate high cycling performance, their capacity utilization is limited owing to mass transport. In addition, static batteries do not possess the advantages of decoupled energy and power of RFBs. A recent study by Meng et al.[24] reported a stirring strategy to enhance mass transport and increase battery capacity utilization. Hence, we adopted a stirring technique (Figure

https://doi.org/10.1021/jacs.4c10106
J. Am. Chem. Soc. XXXX, XXX, XXX−XXX

S22) for the Mg||**TEMPO** (0.5 M) and Mg||**C3-PTZ** (0.5 M) MBSBs, which resulted in improved capacity utilizations of 92.4% for and 93.8%, respectively (Figure 7A,B) (compared to 70.2% and 71.5% for the corresponding static MBSBs). Moreover, both Mg||**TEMPO** (0.5 M) and Mg||**C3-PTZ** (0.5 M) stirred MBSBs were cycled for 200 charge/discharge cycles, exhibiting capacity retention of 99.82% (99.999 per cycle, 99.994 per day) (~35 days) and 99.88% (99.999 per cycle, 99.996 per day) (~39 days), respectively, CE of 99.51% and 99.58%, VE of 92.82% and 93.15%, and EE of 92.36% and 92.78%, respectively. Furthermore, the negligible change in the CV current intensity of the catholytes (Figure 7C,D) and anolytes (Figure S23A,B) demonstrated high stability and negligible crossover of redox-active materials. In addition, EIS analysis of the stirred batteries before and after cycling confirmed stable kinetics (Figure S24A,B). Furthermore, both stirred batteries were investigated in charge rate tests by varying the current density from 10 to 15 mA/cm^2. The Mg||**TEMPO** (0.5 M) and Mg||**C3-PTZ** (0.5 M)-stirred batteries exhibited a slight increase/decrease in the charge/discharge voltage with increasing current density owing to mass-transport limitations (Figure 7E,F). As a result, the Mg||**TEMPO** (0.5 M) and Mg||**C3-PTZ** (0.5 M) stirred batteries operated at higher current densities (12.5, and 15 mA/cm^2) exhibited reduced EE values (Figure 7G,H). However, both batteries regained their initial efficiency values and cycling performance when cycled back at 10 mA/cm^2, demonstrating a high charge/discharge rate behavior. Though stirred batteries demonstrate enhanced mass transport and increased capacity utilization, battery scalability remains limited because of their coupled energy and power characteristics.[22]

To overcome these limitations, we investigated the Mg||**TEMPO** (0.5 M) and Mg||**C3-PTZ** (0.5 M) batteries under flow conditions. A schematic and a digital photograph of the flow setup are shown in Figures 8A and S25, respectively. All the charge/discharge experiments were performed with exposure to air under ambient conditions. This study marks the first demonstration of a Mg-based membrane-free biphasic redox flow battery, enabling the advantage of decoupled energy and power. The flow rates of the batteries were optimized between 1 and 5 mL/min, and both batteries exhibited optimal performances at a flow rate of 3 mL/min (Figure S26). The charge/discharge performance of the batteries was explored over 500 cycles at 12 mA/cm^2 under ambient conditions at an optimized flow rate of 3 mL/min. After 500 charge/discharge cycles, the Mg||**TEMPO** (0.5 M) and Mg||**C3-PTZ** (0.5 M) redox flow MBSBs exhibited capacity utilizations of 92.2% and 91.7%, respectively, retentions of 93.58% (99.987 per cycle, 99.924 per day) (~85 days) and 92.16% (99.984 per cycle, 99.903 per day) (~81 days), CE of 99.8% and 99.7%, VE of 93.5% and 92.2%, and EE of 92.8% and 91.9% (Figure 8B,C). The high-capacity retentions of both batteries were attributed to the negligible crossover of redox-active materials, as confirmed by the CV analysis of the pre- and postcycled catholytes (Figure 8D,E) and anolytes (Figure S27A,B). Excellent self-discharge performance was also observed for both batteries over 170 h (7 days). A low voltage drop over time (0.72 mV/h and 16.3 mV/day for Mg||**TEMPO** and 0.68 mV/h and 15.7 mV/day for Mg||**C3-PTZ**) (Figure S28A,B) further demonstrated high stability of Mg metal anode as well as the catholyte materials. EIS analysis of Mg||**TEMPO** (0.5 M) and Mg||**C3-PTZ** (0.5 M) before and after flow cycling showed no major change in the charge-transfer resistance, suggesting that the kinetics of the system remained intact (Figure S29A,B). These results also confirmed that the Mg metal anode did not form a $Mg(OH)_2$ passivation layer, which was attributed to the excellent stability of the Mg^{2+}-conducting interface and improved Mg reversibility in the aqueous Mg electrolyte. To study the effects of current density on battery performance, Mg||**TEMPO** (0.5 M) and Mg||**C3-PTZ** (0.5 M) batteries were charged/discharged at current densities of 10, 12.5, and 15 mA/cm^2, and the corresponding cycling profiles and Coulombic, voltage, and energy efficiencies were recorded (Figure 8F,G). Both batteries exhibited increased charge/discharge overpotentials when operated at higher current densities of 12.5 and 15 mA/cm^2 owing to mass-transport limitations (Figure 8H,I). Both batteries regained their original performance when cycled back at 10 mA/cm^2, suggesting high rate cyclability under flow conditions.

The power densities were also measured for both batteries under flow conditions. The peak power densities of the Mg||TEMPO (0.5 M) and Mg||C3-PTZ (0.5 M) batteries are 195 and 191 mW/cm^2, respectively (Figure S30A,B), surpassing the power densities of 139 mW/cm^2 for Mg||TEMPO (0.5 M) and 144 mW/cm^2 for Mg||C3-PTZ (0.5 M) under static conditions. The improvement in power density can be attributed to enhanced mass transport under flow conditions. The ASR of the electrolyte and whole cell under flow conditions revealed that the electrolyte resistance contributed to over 70% (Mg||TEMPO) and 65% (Mg||C3-PTZ) of the total battery resistance (Figure S30C,D). Under flow conditions, both the electrolyte and overall ASR notably decreased compared with that of the static MBSBs, enabling higher current and power densities without compromising battery performance.

Economic Analysis. The cost of RFBs plays a pivotal role in their practical application. Generally, the total cost of an RFB includes several key components: the membrane, carbon electrode, active materials, the electrolyte and its salt, bipolar plate, current collector plate, the pump to circulate the electrolyte, gasket, bolts, and end plates.[63,64] The cost distribution among the major components of RFBs varies considerably, with the membrane accounting for 20−30% of the cost, the bipolar plate 15−20%, the carbon electrode 10−15%, active materials (anode and cathode) 20−50%, current collector plate 5−10%, and miscellaneous components such as pumps, end plates, gaskets, and bolts comprising 2−5%.[65,66] The aqueous electrolyte, with its almost negligible cost ($0.1/kg), compose <2% of the total cost of aqueous redox flow batteries (ARFBs, all-vanadium, zinc−bromine, zinc-ferricyanide, etc.).[65] In contrast, the significantly higher cost of a nonaqueous electrolyte ($3/L) and its salt ($5/kg) makes up 20−35% of the total cost of nonaqueous redox flow batteries (NRFB, Li-**TEMPO**).[64,65] These estimations result in a substantial difference in capital costs, for example, the cost of a NRFB (Li-**TEMPO**) at $1237/kW h is five times higher than that of an all-vanadium ARFB at $252/kW h.[65] The present system is an aqueous/nonaqueous membrane-free system, and thus, the cost of a membrane is avoided. It utilizes water and Mg metal ($2/kg) as an inexpensive anolyte phase, and CH_2Cl_2 with the redox materials **TEMPO** and **C3-PTZ** as the catholyte phase. The solvent cost of CH_2Cl_2 (~$20/L)[67] is approximately 60 times lower than carbonate-based nonaqueous electrolytes (~$1200/L).[68] In addition, the costs of the major anolyte and catholyte salts, $MgCl_2$ (~$68/kg)[69] and $TBAPF_6$ (~$2000/kg),[70] are significantly lower than those of

https://doi.org/10.1021/jacs.4c10106
J. Am. Chem. Soc. XXXX, XXX, XXX−XXX

the Li-based salts (LiTFSI at ~$4000/kg,[71] $LiPF_6$ at ~$3800/kg[68]) used in NRFBs. Furthermore, the costs of **TEMPO** ($7000/kg)[72] and **C3-PTZ** (~$133/kg)[28] are comparable to those of the active materials (~$256/kg, vanadium)[73] used in ARFBs. In addition, the developed battery system can be operated under open-air conditions, avoiding the need for an air-free chamber, such as an argon-filled glovebox. Overall, the presented membrane-free system has a significantly lower cost than both all-vanadium ARFBs and **TEMPO**-based NRFBs.

CONCLUSIONS

This study introduced a newly developed high-voltage liquid/liquid membrane-free battery employing a Mg metal anode in both static and flow configurations. This system leverages the advantages of the high voltage and fast kinetics of the Mg metal anode within a biphasic membrane-free flow setup to enable the independent optimization of energy and power. The biphasic system utilizes a CH_2Cl_2 catholyte and an aqueous anolyte containing EG and IL additives to address the passivation issue of Mg metal in traditional electrolyte systems. In addition, a Mg^{2+}-conductive interface was implemented to modify the Mg metal electrode, preventing direct contact between the Mg metal and water molecules to further mitigate the passivation issue. Notably, the batteries operating under ambient atmospheric conditions exhibit remarkable oxygen tolerance. The Mg||**TEMPO** and Mg||**C3-PTZ** batteries were tested under static, stirred, and flow conditions. The initial analysis focused on the charge/discharge performance at different catholyte material concentrations. Notably, the Mg||**TEMPO** (0.5 M) and Mg||**C3-PTZ** (0.5 M) batteries exhibited exceptional performance over 500 cycles, with capacity retention rates of 97.84% and 98.87%, respectively, (under static conditions) and 93.58% and 92.16% (under flow conditions). In addition, both Mg||**TEMPO** (0.5 M) and Mg||**C3-PTZ** (0.5 M) under flow conditions outperformed the power performance in the static configuration, with power densities of 195 and 191 mW/cm^2, respectively. Overall, the newly developed cost-effective Mg MBSBs exhibited remarkable battery performance, paving the way for innovative applications of Mg chemistry in flow batteries.

ASSOCIATED CONTENT

Supporting Information

The Supporting Information is available free of charge at https://pubs.acs.org/doi/10.1021/jacs.4c10106.

Additional calculation results, experimental details, materials, methods, and characterization data (PDF)

AUTHOR INFORMATION

Corresponding Author

Jianbing Jimmy Jiang − *Department of Chemistry, University of Cincinnati, Cincinnati, Ohio 45221, United States;* orcid.org/0000-0002-7466-522X; Email: jianbing.jiang@uc.edu

Authors

Rajeev K. Gautam − *Department of Chemistry, University of Cincinnati, Cincinnati, Ohio 45221, United States*

Jack J. McGrath − *Department of Chemistry, University of Cincinnati, Cincinnati, Ohio 45221, United States*

Xiao Wang − *Department of Chemistry, University of Cincinnati, Cincinnati, Ohio 45221, United States*

Complete contact information is available at: https://pubs.acs.org/10.1021/jacs.4c10106

Author Contributions

The manuscript was written through contributions of all authors.

Notes

The authors declare no competing financial interest.

ACKNOWLEDGMENTS

This work is supported by the National Science Foundation under grant no. CBET-2112798.

REFERENCES

(1) Dunn, B.; Kamath, H.; Tarascon, J. M. Electrical energy storage for the grid: A battery of choices. *Science* **2011**, *334* (6058), 928−935.

(2) Larcher, D.; Tarascon, J. M. Towards greener and more sustainable batteries for electrical energy storage. *Nat. Chem.* **2015**, *7* (1), 19−29.

(3) Kittner, N.; Lill, F.; Kammen, D. M. Energy storage deployment and innovation for the clean energy transition. *Nat. Energy* **2017**, *2* (9), 17125.

(4) Tian, Y.; Zeng, G.; Rutt, A.; Shi, T.; Kim, H.; Wang, J.; Koettgen, J.; Sun, Y.; Ouyang, B.; Chen, T.; Lun, Z.; Rong, Z.; Persson, K.; Ceder, G. Promises and challenges of next-generation "beyond Li-ion" batteries for electric vehicles and grid decarbonization. *Chem. Rev.* **2021**, *121* (3), 1623−1669.

(5) Masias, A.; Marcicki, J.; Paxton, W. A. Opportunities and challenges of lithium ion batteries in automotive applications. *ACS Energy Lett.* **2021**, *6* (2), 621−630.

(6) Winter, M.; Barnett, B.; Xu, K. Before Li ion batteries. *Chem. Rev.* **2018**, *118* (23), 11433−11456.

(7) Saha, P.; Datta, M. K.; Velikokhatnyi, O. I.; Manivannan, A.; Alman, D.; Kumta, P. N. Rechargeable magnesium battery: Current status and key challenges for the future. *Prog. Mater. Sci.* **2014**, *66*, 1−86.

(8) Leong, K. W.; Pan, W.; Wang, Y.; Luo, S.; Zhao, X.; Leung, D. Y. C. Reversibility of a high-voltage, Cl^--regulated, aqueous Mg metal battery enabled by a water-in-salt electrolyte. *ACS Energy Lett.* **2022**, *7* (8), 2657−2666.

(9) Liu, F.; Wang, T.; Liu, X.; Fan, L. Z. Challenges and recent progress on key materials for rechargeable magnesium batteries. *Adv. Energy Mater.* **2020**, *11* (2), 2000787.

(10) Qin, Y.; Holguin, K.; Fehlau, D.; Luo, C.; Gao, T. Nonaqueous Mg flow battery with a polymer catholyte. *ACS Appl. Energy Mater.* **2022**, *5* (3), 2675−2678.

(11) He, P.; Ford, H. O.; Gonzalez, S.; Rodriguez, S.; Oliver, A. G.; Schaefer, J. L. Stability and disproportionation of magnesium polysulfides and the effects on the Mg-polysulfide flow battery. *J. Electrochem. Soc.* **2021**, *168* (11), 110516.

(12) Soloveichik, G. L. Flow batteries: Current status and trends. *Chem. Rev.* **2015**, *115* (20), 11533−11558.

(13) Hou, S.; Chen, L.; Fan, X.; Fan, X.; Ji, X.; Wang, B.; Cui, C.; Chen, J.; Yang, C.; Wang, W.; Li, C.; Wang, C. High-energy and low-cost membrane-free chlorine flow battery. *Nat. Commun.* **2022**, *13* (1), 1281.

(14) Ye, C.; Tan, R.; Wang, A.; Chen, J.; Comesana Gandara, B.; Breakwell, C.; Alvarez-Fernandez, A.; Fan, Z.; Weng, J.; Bezzu, C. G.; Guldin, S.; Brandon, N. P.; Kucernak, A. R.; Jelfs, K. E.; McKeown, N. B.; Song, Q. Long-life aqueous organic redox flow batteries enabled by amidoxime-functionalized ion-selective polymer membranes. *Angew. Chem., Int. Ed.* **2022**, *61* (38), No. e202207580.

(15) Liang, Y.; Dong, H.; Aurbach, D.; Yao, Y. Current status and future directions of multivalent metal-ion batteries. *Nat. Energy* **2020**, *5* (9), 646−656.

(16) Deivanayagam, R.; Ingram, B. J.; Shahbazian-Yassar, R. Progress in development of electrolytes for magnesium batteries. *Energy Storage Mater.* **2019**, *21*, 136−153.
(17) Wang, Z.; Zhou, J.; Ji, H.; Liu, J.; Zhou, Y.; Qian, T.; Yan, C. Principles and design of biphasic self-stratifying batteries toward next-generation energy storage. *Angew. Chem., Int. Ed.* **2024**, *63* (20), No. e202320258.
(18) Navalpotro, P.; Trujillo, C.; Montes, I.; Neves, C. M. S. S.; Palma, J.; Freire, M. G.; Coutinho, J. A. P.; Marcilla, R. Critical aspects of membrane-free aqueous battery based on two immiscible neutral electrolytes. *Energy Storage Mater.* **2020**, *26*, 400−407.
(19) Navalpotro, P.; Sierra, N.; Trujillo, C.; Montes, I.; Palma, J.; Marcilla, R. Exploring the versatility of membrane-free battery concept using different combinations of immiscible redox electrolytes. *ACS Appl. Mater. Interfaces* **2018**, *10* (48), 41246−41256.
(20) Peljo, P.; Bichon, M.; Girault, H. H. Ion transfer battery: Storing energy by transferring ions across liquid-liquid interfaces. *Chem. Commun.* **2016**, *52* (63), 9761−9764.
(21) Xu, P.; Xie, C.; Wang, C.; Lai, Q.; Wang, W.; Zhang, H.; Li, X. A membrane-free interfacial battery with high energy density. *Chem. Commun.* **2018**, *54* (82), 11626−11629.
(22) Navalpotro, P.; Palma, J.; Anderson, M.; Marcilla, R. A membrane-free redox flow battery with two immiscible redox electrolytes. *Angew. Chem., Int. Ed.* **2017**, *56* (41), 12460−12465.
(23) Navalpotro, P.; Neves, C.; Palma, J.; Freire, M. G.; Coutinho, J. A. P.; Marcilla, R. Pioneering use of ionic liquid-based aqueous biphasic systems as membrane-free batteries. *Adv. Sci.* **2018**, *5* (10), 1800576.
(24) Meng, J.; Tang, Q.; Zhou, L.; Zhao, C.; Chen, M.; Shen, Y.; Zhou, J.; Feng, G.; Shen, Y.; Huang, Y. A stirred self-stratified battery for large-scale energy storage. *Joule* **2020**, *4* (4), 953−966.
(25) Wang, Z.; Ji, H.; Zhou, J.; Zheng, Y.; Liu, J.; Qian, T.; Yan, C. Exploiting nonaqueous self-stratified electrolyte systems toward large-scale energy storage. *Nat. Commun.* **2023**, *14* (1), 2267.
(26) Chakraborty, A.; Bock, R.; Green, R.; Luker, K.; Ménard, G.; Sepunaru, L. Split biphasic electrochemical cells: Toward membraneless redox flow batteries. *ACS Appl. Energy Mater.* **2023**, *6* (2), 605−610.
(27) Chai, J.; Lashgari, A.; Eisenhart, A. E.; Wang, X.; Beck, T. L.; Jiang, J. Biphasic, membrane-free Zn/phenothiazine battery: effects of hydrophobicity of redox materials on cyclability. *ACS Mater. Lett.* **2021**, *3* (4), 337−343.
(28) Gautam, R. K.; Wang, X.; Lashgari, A.; Sinha, S.; McGrath, J.; Siwakoti, R.; Jiang, J. Development of high-voltage and high-energy membrane-free nonaqueous lithium-based organic redox flow batteries. *Nat. Commun.* **2023**, *14* (1), 4753.
(29) Wang, X.; Lashgari, A.; Chai, J.; Jiang, J. A membrane-free, aqueous/nonaqueous hybrid redox flow battery. *Energy Storage Mater.* **2022**, *45*, 1100−1108.
(30) Gautam, R. K.; Wang, X.; Sinha, S.; Jiang, J. Triphasic electrolytes for membrane-free high-voltage redox flow battery. *ACS Energy Lett.* **2024**, *9* (1), 218−225.
(31) Navalpotro, P.; Ibañez, S. E.; Pedraza, E.; Marcilla, R. A neutral pH aqueous biphasic system applied to both static and flow membrane-free battery. *Energy Storage Mater.* **2023**, *56*, 403−411.
(32) Pour, N.; Gofer, Y.; Major, D. T.; Aurbach, D. Structural analysis of electrolyte solutions for rechargeable Mg batteries by stereoscopic means and DFT calculations. *J. Am. Chem. Soc.* **2011**, *133* (16), 6270−6278.
(33) Gao, T.; Hou, S.; Wang, F.; Ma, Z.; Li, X.; Xu, K.; Wang, C. Reversible S0/MgSx Redox Chemistry in a MgTFSI2/MgCl2/DME Electrolyte for Rechargeable Mg/S Batteries. *Angew. Chem., Int. Ed.* **2017**, *56* (43), 13526−13530.
(34) Canepa, P.; Jayaraman, S.; Cheng, L.; Rajput, N. N.; Richards, W. D.; Gautam, G. S.; Curtiss, L. A.; Persson, K. A.; Ceder, G. Elucidating the structure of the magnesium aluminum chloride complex electrolyte for magnesium-ion batteries. *Energy Environ. Sci.* **2015**, *8* (12), 3718−3730.
(35) See, K. A.; Chapman, K. W.; Zhu, L.; Wiaderek, K. M.; Borkiewicz, O. J.; Barile, C. J.; Chupas, P. J.; Gewirth, A. A. The Interplay of Al and Mg speciation in advanced Mg battery electrolyte solutions. *J. Am. Chem. Soc.* **2016**, *138* (1), 328−337.
(36) He, S.; Luo, J.; Liu, T. L. $MgCl_2/AlCl_3$ electrolytes for reversible Mg deposition/stripping: electrochemical conditioning or not? *J. Mater. Chem. A* **2017**, *5* (25), 12718−12722.
(37) Kim, S. S.; Bevilacqua, S. C.; See, K. A. Conditioning-free Mg electrolyte by the minor addition of $Mg(HMDS)_2$. *ACS Appl. Mater. Interfaces* **2020**, *12* (5), 5226−5233.
(38) Liao, C.; Sa, N.; Key, B.; Burrell, A. K.; Cheng, L.; Curtiss, L. A.; Vaughey, J. T.; Woo, J.-J.; Hu, L.; Pan, B.; Zhang, Z. The unexpected discovery of the $Mg(HMDS)_2/MgCl_2$ complex as a magnesium electrolyte for rechargeable magnesium batteries. *J. Mater. Chem. A* **2015**, *3* (11), 6082−6087.
(39) Shterenberg, I.; Salama, M.; Yoo, H. D.; Gofer, Y.; Park, J.-B.; Sun, Y.-K.; Aurbach, D. Evaluation of $(CF_3SO_2)_2N^-$(TFSI) based electrolyte solutions for Mg batteries. *J. Electrochem. Soc.* **2015**, *162* (13), A7118−A7128.
(40) Mohtadi, R.; Tutusaus, O.; Arthur, T. S.; Zhao-Karger, Z.; Fichtner, M. The metamorphosis of rechargeable magnesium batteries. *Joule* **2021**, *5* (3), 581−617.
(41) Ng, K. L.; Shu, K.; Azimi, G. A rechargeable $Mg|O_2$ battery. *iScience* **2022**, *25* (8), 104711.
(42) Vardar, G.; Sleightholme, A. E.; Naruse, J.; Hiramatsu, H.; Siegel, D. J.; Monroe, C. W. Electrochemistry of magnesium electrolytes in ionic liquids for secondary batteries. *ACS Appl. Mater. Interfaces* **2014**, *6* (20), 18033−18039.
(43) Chellappan, L. K.; Kvello, J.; Tolchard, J. R.; Dahl, P. I.; Hanetho, S. M.; Berthelot, R.; Fiksdahl, A.; Jayasayee, K. Non-nucleophilic electrolyte based on ionic liquid and magnesium bis(diisopropyl)amide for rechargeable magnesium-ion batteries. *ACS Appl. Energy Mater.* **2020**, *3* (10), 9585−9593.
(44) Kakibe, T.; Hishii, J.-y.; Yoshimoto, N.; Egashira, M.; Morita, M. Binary ionic liquid electrolytes containing organo-magnesium complex for rechargeable magnesium batteries. *J. Power Sources* **2012**, *203*, 195−200.
(45) Watkins, T.; Kumar, A.; Buttry, D. A. Designer ionic liquids for reversible electrochemical deposition/dissolution of magnesium. *J. Am. Chem. Soc.* **2016**, *138* (2), 641−650.
(46) Tan, J.; Liu, J. Electrolyte engineering toward high-voltage aqueous energy storage devices. *Energy Environ. Mater.* **2021**, *4* (3), 302−306.
(47) Wang, F.; Fan, X.; Gao, T.; Sun, W.; Ma, Z.; Yang, C.; Han, F.; Xu, K.; Wang, C. High-voltage aqueous magnesium ion batteries. *ACS Cent. Sci.* **2017**, *3* (10), 1121−1128.
(48) Fu, Q.; Wu, X.; Luo, X.; Indris, S.; Sarapulova, A.; Bauer, M.; Wang, Z.; Knapp, M.; Ehrenberg, H.; Wei, Y.; Dsoke, S. High-voltage aqueous Mg-ion batteries enabled by solvation structure reorganization. *Adv. Funct. Mater.* **2022**, *32* (16), 2110674.
(49) Shen, Y.; Liu, B.; Liu, X.; Liu, J.; Ding, J.; Zhong, C.; Hu, W. Water-in-salt electrolyte for safe and high-energy aqueous battery. *Energy Storage Mater.* **2021**, *34*, 461−474.
(50) Ma, Z.; Kar, M.; Xiao, C.; Forsyth, M.; MacFarlane, D. R. Electrochemical cycling of Mg in $Mg[TFSI]_2$/tetraglyme electrolytes. *Electrochem. Commun.* **2017**, *78*, 29−32.
(51) Zhang, Y.; Ye, R.; Henkensmeier, D.; Hempelmann, R.; Chen, R. Water-in-ionic liquid" solutions towards wide electrochemical stability windows for aqueous rechargeable batteries. *Electrochim. Acta* **2018**, *263*, 47−52.
(52) Xie, J.; Liang, Z.; Lu, Y. C. Molecular crowding electrolytes for high-voltage aqueous batteries. *Nat. Mater.* **2020**, *19* (9), 1006−1011.
(53) Huang, S.; Li, Z.; Li, P.; Du, X.; Ma, M.; Liang, Z.; Su, Y.; Xiong, L. Ultrahigh-voltage aqueous electrolyte for wide-temperature supercapacitors. *J. Mater. Chem. A* **2023**, *11* (28), 15532−15539.
(54) Song, G.; StJohn, D. Corrosion behaviour of magnesium in ethylene glycol. *Corros. Sci.* **2004**, *46* (6), 1381−1399.

https://doi.org/10.1021/jacs.4c10106
J. Am. Chem. Soc. XXXX, XXX, XXX−XXX

(55) Lopez, J.; Pei, A.; Oh, J. Y.; Wang, G. J. N.; Cui, Y.; Bao, Z. Effects of polymer coatings on electrodeposited lithium metal. *J. Am. Chem. Soc.* **2018**, *140* (37), 11735−11744.
(56) Wang, Y.; Wang, Y.; Chen, C.; Chen, X.; Zhao, Q.; Yang, L.; Yao, L.; Qin, R.; Wu, H.; Jiang, Z.; Pan, F. Optimizing the sulfonic groups of a polymer to coat the zinc anode for dendrite suppression. *Chem. Commun.* **2021**, *57* (43), 5326−5329.
(57) Wu, Q.; Shu, K.; Sun, L.; Wang, H. Recent advances in non-nucleophilic Mg electrolytes. *Front. Mater.* **2021**, *7*, 612134.
(58) Nguyen, D.-T.; Eng, A. Y. S.; Ng, M.-F.; Kumar, V.; Sofer, Z.; Handoko, A. D.; Subramanian, G. S.; Seh, Z. W. A high-performance magnesium triflate-based electrolyte for rechargeable magnesium batteries. *Cell Rep. Phys. Sci.* **2020**, *1* (12), 100265.
(59) Chen, J.; Tan, S.; Li, L.; Huang, G.; Wang, J.; Pan, F. The Metamorphosis of $Mg(SO_3CF_3)_2$-based electrolytes for rechargeable magnesium batteries. *ChemElectroChem* **2024**, *11* (8), No. e202300664.
(60) Bard, A. J.; Faulkner, L. R.; White, H. S. *Electrochemical Methods: Fundamentals and Applications*; John Wiley & Sons, 2022.
(61) Huskinson, B.; Marshak, M. P.; Suh, C.; Er, S.; Gerhardt, M. R.; Galvin, C. J.; Chen, X.; Aspuru-Guzik, A.; Gordon, R. G.; Aziz, M. J. A metal-free organic-inorganic aqueous flow battery. *Nature* **2014**, *505* (7482), 195−198.
(62) Yang, B.; Hoober-Burkhardt, L.; Wang, F.; Surya Prakash, G. K.; Narayanan, S. R. An inexpensive aqueous flow battery for large-scale electrical energy storage based on water-soluble organic redox couples. *J. Electrochem. Soc.* **2014**, *161* (9), A1371−A1380.
(63) Darling, R. M. Techno-economic analyses of several redox flow batteries using levelized cost of energy storage. *Curr. Opin. Chem. Eng.* **2022**, *37*, 100855.
(64) Li, Z.; Fang, X.; Cheng, L.; Wei, X.; Zhang, L. Techno-economic analysis of non-aqueous hybrid redox flow batteries. *J. Power Sources* **2022**, *536*, 231493.
(65) Tang, L.; Leung, P.; Mohamed, M. R.; Xu, Q.; Dai, S.; Zhu, X.; Flox, C.; Shah, A. A.; Liao, Q. Capital cost evaluation of conventional and emerging redox flow batteries for grid storage applications. *Electrochim. Acta* **2023**, *437*, 141460.
(66) Minke, C.; Dorantes Ledesma, M. A. Impact of cell design and maintenance strategy on life cycle costs of vanadium redox flow batteries. *J. Energy Storage* **2019**, *21*, 571−580.
(67) Sigma-Aldrich. www.sigmaaldrich.com/US/en/product/sigma/l090001 (accessed 04-14, 2024).
(68) Sigma-Aldrich. www.sigmaaldrich.com/US/en/product/aldrich/746738 (accessed 04-14, 2024).
(69) Sigma-Aldrich. www.sigmaaldrich.com/US/en/product/sigma/m8266 (accessed 04-14, 2024).
(70) Sigma-Aldrich. www.sigmaaldrich.com/US/en/product/aldrich/281026 (accessed 04-14, 2024).
(71) Sigma-Aldrich. www.sigmaaldrich.com/US/en/product/aldrich/544094 (accessed 04-14, 2024).
(72) Sigma-Aldrich. www.sigmaaldrich.com/US/en/product/aldrich/214000 (accessed 04-14, 2024).
(73) Sigma-Aldrich. www.sigmaaldrich.com/US/en/product/aldrich/221899 (accessed 04-14, 2024).

https://doi.org/10.1021/jacs.4c10106
J. Am. Chem. Soc. XXXX, XXX, XXX−XXX